Nanoscale

COMMUNICATION

View Article Online
View Journal | View Issue

Check for updates

Cite this: *Nanoscale*, 2024, **16**, 11959

Received 22nd November 2023,
Accepted 24th March 2024

DOI: 10.1039/d3nr05947b

rsc.li/nanoscale

In vivo biodistribution and tumor uptake of [^{64}Cu]-FAU nanozeolite *via* positron emission tomography Imaging†

Charly Hélaine, ‡[a] Abdallah Amedlous, ‡[b] Jérôme Toutain,[a] Carole Brunaud,[a] Oleg Lebedev,[c] Charlotte Marie,[d] Cyrille Alliot,[e,f] Myriam Bernaudin,[a] Ferid Haddad,[f,g] Svetlana Mintova *§[b] and Samuel Valable *§[a]

Nanoparticles have emerged as promising theranostic tools for biomedical applications, notably in the treatment of cancers. However, to fully exploit their potential, a thorough understanding of their biodistribution is imperative. In this context, we prepared radioactive [^{64}Cu]-exchanged faujasite nanosized zeolite ([^{64}Cu]-FAU) to conduct positron emission tomography (PET) imaging tracking in preclinical glioblastoma models. *In vivo* results revealed a rapid and gradual accumulation over time of intravenously injected [^{64}Cu]-FAU zeolite nanocrystals within the brain tumor, while no uptake in the healthy brain was observed. Although a specific tumor targeting was observed in the brain, the kinetics of uptake into tumor tissue was found to be dependent on the glioblastoma model. Indeed, our results showed a rapid uptake in U87-MG model while in U251-MG glioblastoma model tumor uptake was gradual over the time. Interestingly, a [^{64}Cu] activity, decreasing over time, was also observed in organs of elimination such as kidney and liver without showing a difference in activity between both glioblastoma models. *Ex vivo* analyses confirmed the presence of zeolite nanocrystals in brain tumor with detection of both Si and Al elements originated from them. This radiolabelling strategy, performed for the first time using nanozeolites, enables precise tracking through PET imaging and confirms their accumulation within the glioblastoma. These findings further bolster the potential use of zeolite nanocrystals as valuable theranostic tools.

Introduction

Nanoparticles are increasingly employed in the field of biomedicine in recent years and mostly in cancer imaging (diagnosis), and/or cancer treatment (therapy) making them appealing theranostic tools.[1] The use of nanoparticles as carriers for desired drugs and gases to treat brain diseases is increasingly investigated,[2,3] particularly in situations where the blood–brain barrier is disrupted, which permits nanoparticles to reach the brain parenchyma through the enhanced permeability and retention (EPR) effect. Among these situations, one cites brain tumors, in which hypoxia is a hallmark, notably for the glioblastoma (GBM), and for which the use of nanoparticles as oxygen carrier has increased owing to their high versatility and designed synthesis approaches that enable modification of their properties for particular uses.[3] Over the various biocompatible nanoparticles, zeolites, and particularly faujasite-type zeolite (FAU) have demonstrated the ability to act as oxygen/carbogen carriers.[4] This performance is ascribed to the microporous nature of zeolite, which possesses an exceptional capacity for oxygen storage and release. Additionally, nanosized zeolites exhibit a range of advantageous properties, such as a high surface area, excellent ion exchange capacity, remarkable colloidal stability, and biocompatibility.[4–6] These characteristics make them highly promising with multiple functionalities, particularly important for biomedical applications.[7] For example, the ion exchange ability of nanozeolites with various cations such Fe^{3+}, Cu^{2+}, Gd^{3+} enhances their functioning as drug or gases carrier and imaging tools including magnetic resonance imaging (MRI) and positron emission imaging (PET).[4,8–10] Both tools are well adapted for biomedical imaging in neuro-oncology.[11]

Previously, our group reported that in glioblastoma models, Gd-containing FAU zeolite nanoparticles can be specifically detected by *T*1w-MRI in the tumor, but not in the normal brain tissue.[4] However, performing a whole-body examination and tracking with MRI remains challenging. Indeed, overtime, the nanoparticles will diffuse within the tissue, causing a decrease in local Gd concentration, which makes detecting the

[a]*Université de Caen Normandie, CNRS, Normandie Université, ISTCT UMR6030, GIP CYCERON, F-14000 Caen, France. E-mail: samuel.valable@cnrs.fr*
[b]*Université de Caen Normandie, ENSICAEN, CNRS, Normandie Université, Laboratoire Catalyse et Spectrochimie (LCS), F-14050 Caen, France. E-mail: svetlana.mintova@ensicaen.fr*
[c]*Université de Caen Normandie, ENSICAEN, CNRS, Normandie Université, Laboratoire de Cristallographie et Science des Matériaux (CRISMAT), F-14050 Caen, France*
[d]*UAR3408/US50, Université de Caen Normandie, CNRS, INSERM, CEA, GIP CYCERON, F-14000 Caen, France*
[e]*CRCI2NA, Inserm, CNRS, Nantes Université, F-44007 Nantes Cedex 1, France*
[f]*GIP ARRONAX, F-44800 Saint-Herblain, France*
[g]*IMT Atlantique, Nantes Université, CNRS, Subatech, F-44000 Nantes, France*
†Electronic supplementary information (ESI) available. See DOI: https://doi.org/10.1039/d3nr05947b
‡These authors contributed equally to the work and should be considered co-first authors.
§Equal contribution.

nanoparticles even more difficult. Nonetheless, achieving quantitative and absolute tracking of nanoparticles in the targeted tissue and throughout the body remains challenging and requires further investigations, notably with MRI.

PET imaging, in contrast to MRI, can provide quantitative assessment of nanoparticles *in vivo* with high sensitivity. It, indeed, requires lower concentrations of radionuclides compared to paramagnetic compound required for MRI. Various positron-emitting radionuclides are available for PET imaging with the most common one being [^{18}F] ($T_{1/2}$ = 109 min). However, its relative short half-life is not well-suited for prolonged biodistribution studies and therefore nanoparticles tracking is problematic. Over the last decade, numerous other radioisotopes have been developed for biomedical use. Among these, [^{64}Cu] is particularly interesting for PET studies due to its nuclear properties.[12] Apart from its distinct decay modes, including electron capture (41%), positron emission (19%) and β emission (40%), its long half-life of 12.7 hours enables *in vivo* imaging studies for several hours even days after injection.[13]

Different strategies make it possible to radiolabel nanoparticles, with the most common one being the use of bifunctional chelators.[14] However, this approach is beset by challenges, including the potential detachment of radiometals and alterations in the surface properties of the nanoparticles. Exploiting the ion exchange characteristics of zeolite, radiolabelled zeolite A with high atomic weight radionuclides cations (Na^+ or K^+) were reported.[15–18]

In this study, we present the loading of FAU zeolite nanocrystals in colloidal suspension with radioisotope copper-64 [^{64}Cu] using [^{64}Cu]-Cl_2. The material, denoted as [^{64}Cu]-FAU, is used to evaluate the zeolite biodistribution allowing a quantitative evaluation of the uptake of the zeolite nanocrystals in preclinical glioblastoma model at different post-injection times.

The rapid accumulation of [^{64}Cu]-FAU zeolite nanocrystals with strong specificity for brain tumors, lasting at least 48 hours is demonstrated. The localization of zeolite nanocrystals within the tumor is confirmed additionally by energy dispersive X-ray (EDX) analysis.

Experimental

Chemicals

Sodium hydroxide pellets (NaOH, 98%) and colloidal silica (SiO_2, Ludox HS30, 30) were purchased from Sigma-Aldrich (Sigma-Aldrich; St Quentin Fallavier, France). Aluminium powder (325 mesh, 99.5%) was purchased from Alfa Aesar. Radioactive copper chloride ([^{64}Cu]-Cl_2) was produced by the GIP ARRONAX (Saint-Herblain, France). All reagents were used as received without further purification. Mili-Q water was used for all synthesis and purification of samples.

Preparation of [^{64}Cu]-FAU zeolite nanocrystals

Faujasite (Na-FAU) zeolite nanocrystals with Si/Al ratio of 1.3 and particle size below 30 nm were synthetized from a clear colloidal precursor suspension, following the previously described procedure.[5] The resulting nanocrystals were stabilized in water suspension with a weight concentration of 2.5 wt%.

The [^{64}Cu]-FAU sample was prepared by ion-exchange method using [4–20] μM of radioactive copper chloride ([^{64}Cu]-Cl_2) mixed with 5 mL of Na-FAU suspension (concentration of 2.5 wt% solid zeolite nanoparticles). The ion-exchange process was performed at room temperature under stirring for 1 hour. Afterward, the sample was purified with water using high speed centrifugation (15 300 rpm, 40 min) and finally stored in the form of a colloidal suspension. Following the ion exchange procedure, a radioactive suspension of [^{64}Cu]-FAU was obtained, containing approximately 50% of the initial [^{64}Cu] activity (Fig. 1).

Characterization of nanosized [^{64}Cu]-FAU zeolite

XRD patterns were measured using a PANalytical X'Pert Pro diffractometer with Cuα monochromatized radiation (λ = 1.5418 Å, 35 kV, 40 mA). The samples were scanned in the 4–60° 2Theta range with a step size of 0.0167°.

The morphology and size of zeolite nanoparticles were characterized using high-resolution transmission electron microscopy (HRTEM) employing an FEI Tecnai G2 30 microscope operating at an accelerating voltage of 300 kV, equipped with a LaB_6 filament.

Particle size distribution in the colloidal zeolite suspensions was measured by Dynamic light scattering (DLS) using a Malvern Zetasizer Nano instrument. The surface charge of the zeolite nanocrystals was characterized by zeta potential measurements of the corresponding suspensions.

Cell lines

Two human glioblastoma-derived cell lines, U251-MG (Cellosaurus CVCL_0021), purchased from the National Cancer Institute (NCI, Bethesda, MD, USA) and U87-MG (Cellosaurus CVCL_0022), purchased from the American Type Culture Collection (ATCC, LGC standards, Molsheim, France), were used in this study. Cells were cultured in DMEM 1 g L^{-1} of glucose (Sigma-Aldrich), supplemented with 10% fetal calf serum (Eurobio, Courtaboeuf, France), 2 mM L-glutamine (Sigma-Aldrich), 100 U mL^{-1} penicillin and 100 μg mL^{-1} streptomycin (Sigma-Aldrich). The cultures were maintained at 37 °C in 5% CO_2 and 95% air.

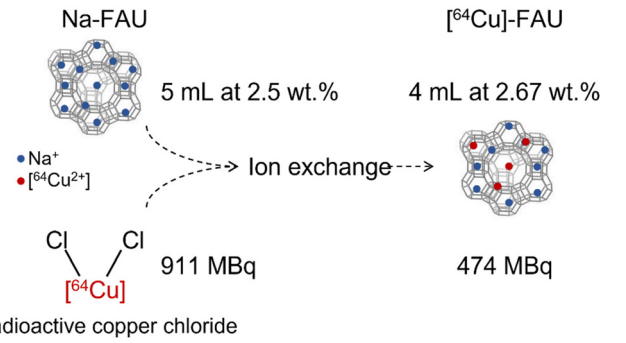

Fig. 1 Schematic representation of the radio-labeling process of zeolite nanocrystals obtained *via* ion exchange procedure.

Animal studies

Animal investigations were conducted in accordance with the current European directive (2010/63/EU). Ethical approval was obtained by S.V from the regional committee (CENOMEXA) and the French Ministère de l'Enseignement Supérieur, de la Recherche et de l'Innovation with the authorization APAFIS#12727.

GBM models

Six-week-old nude male and female rats (250–350 g, CURB, Caen) were used for the study. Rats were housed at the Specific-pathogen-free ONCOModels platform (CYCERON, Caen, France).

Rats were anesthetized with 5% isoflurane for induction and 2% during surgery in a mixture of 70% N_2O and 30% O_2. The depth of anesthesia was assessed beforehand by the foot reflex. Subsequently, the rats were placed in a stereotactic frame after the application of xylocaine gel to the ear bars. A burr hole with a diameter of 1 mm was drilled into the skull at coordinates 3 mm lateral, 0 mm anteroposterior, and 6 mm depth from the Bregma reference point.

U87-MG and U251-MG cells (5×10^4 cells in 3 μL) were injected using a dental needle (30G; 0.3 × 23 mm) at a flow rate of 0.6 μL min^{-1} for 5 min. The needle was withdrawn after 5 min to prevent cell reflux. Upon completing the procedure, the animal was sutured and painkilled (Buprecare® 0.05 mg kg^{-1}, subcutaneously).

Preclinical magnetic resonance imaging (MRI)

MRI scans were performed on a hybrid PET/7T MRI system (Bruker, CYCERON biomedical imaging platform, Caen, France), once a week to monitor tumor development and before each PET acquisition. For all MRI experiments, rats were under anaesthesia (5% isoflurane for induction, 2% for maintenance, in 70% N_2O/30% O_2) were placed in a prone position. Respiration was monitored using a pressure sensitive balloon around the abdomen. After a localizer imaging, an anatomical exploration of the brain was performed using a *T*2w sequence (RARE with acceleration factor of 8; TR/TE = 5000/65 ms; experiments average = 2; 20 contiguous slices; field of view (FOV): 38.4 × 38.4 × 15; matrix: 256 × 256 × 20; resolution: 0.150 × 0.150 × 0.75; acquisition time = 4 min). TR and TE are respectively repetition time and echo time.

A *T*1 FISP-3D (fast imaging with steady-state precession 3D) sequence was employed just before PET acquisition to generate the attenuation map. For brain acquisitions, the parameters were: TR/TE = 5/2.4 ms; average = 2; FOV: 50 × 50 × 80, matrix: 128 × 128 × 92; resolution: 0.39 × 0.39 × 0.87. For whole-body acquisitions: TR/TE = 5/2.4 ms; average = 1; FOV: 60 × 60 × 112.5, matrix: 128 × 128 × 180; resolution: 0.468 × 0.468 × 0.625.

Cerebrovascular parameters were measured 24 hours post-injection in the U87-MG and U251-MG models. Before injecting the contrast agent, *T*2*w (TR/TE = 20 000/14.0 ms, experiments average = 1, 10 contiguous slices, field of view (FOV): 31.5 × 25 × 15; matrix: 100 × 80 × 50; resolution: 0.315 × 0.3125 × 0.3; acquisition time = 3 min 20 s) and *T*2w (using the same parameters as above) were acquired. Two minutes after the injection of P904® (200 μmol kg^{-1}, Guerbet, Villepinte, France), a second *T*2*w scan was acquired.

Cerebral Blood Volume (CBV) maps (expressed in a percentage) were computed from $\Delta R2^*$ and $\Delta\chi$ according to eqn (1):

$$\mathrm{CBV}(\%) = \frac{3}{4\pi} \cdot \left(\frac{\Delta R2^*}{\gamma \cdot \Delta\chi \cdot B_0} \right) \quad (1)$$

where $\Delta R2^*$ represents the difference between relaxation rates before and after the administration of P904®; $\Delta\chi$ is the increase in the magnetic susceptibility difference between the extravascular and intravascular compartments (non-rationalized units) caused by the presence of the contrast agent in the vasculature; B_0 is the main magnetic field in Tesla (T), and γ is the gyromagnetic ratio of protons. Voxels for which no reliable analysis could be performed were omitted (*e.g.*, CBV values outside the range of validity of the method, *i.e.*, fCBV > 20%; negative $\Delta R2^*$).[19]

Preclinical positron emission tomography (PET)

Immediately prior the PET imaging, a *T*2w anatomical sequence was acquired to detect the tumor location using the hybrid PET/7T MRI system (Bruker, CYCERON biomedical imaging platform, Caen, France). The animals were automatically transferred into the PET rings using the animal transport system (ATS; Bruker) to align PET images with MRI images. Radioactive [^{64}Cu]-FAU zeolite was injected into the caudal vein with an average dose of 24 MBq per rat corresponding to a concentration range of 5 to 20 mg kg^{-1} of zeolite suspension. At the time of injection, a static acquisition centered in the head was acquired for 30 min starting at the time of injection. At the end of the acquisition, a second PET acquisition lasting 20 min was also acquired for the lower part of the body, covering the lungs, liver, spleen, kidneys, stomach and up to the colon.

Decay-corrected PET images were reconstructed by the iterative maximum *a posteriori* (MAP) algorithm with corrections for PVC, PSF, scatter, and diffusion. The matrix size of the reconstructed images was 180 × 180 × 198 with a field of view (FOV) of 90 × 90 × 99 mm and a resolution of 0.5 × 0.5 × 0.5 mm. Image analysis is presented for each region of interest (ROI) in terms of SUV_{peak}. SUV_{peak}, suggested as a more robust alternative,[20] is defined as the average SUV within a region of 9 voxels centered on high uptake value (SUV_{max}) part of the ROI.

Biodistribution

At the end of experiments, animals were euthanized under anaesthesia; blood, brain tumor, healthy brain hemisphere, liver, spleen, kidney, lungs and heart were harvested. Each tissue was weighed and its radioactivity was measured using a gamma counter (WIZARD2, PerkinElmer Life Sciences, Gaithersburg, US).

Radioactivity concentrations were corrected by background subtraction and by decay correction, and expressed as percentage of the injected dose per gram of tissue (%ID g^{-1}).

Immunohistofluorescence

Rats were deeply anesthetized and transcardially perfused with cold heparinized saline solution. Brains were removed and immediately snap-frozen in *n*-pentane (Sigma-Aldrich) and stored at −80 °C. Thereafter, brains were cut on a cryostat to obtain coronal sections of 20 µm. Brain sections were collected on superfrost slides (Thermo Fisher Scientific, Illkirch-Graffenstaden, France) and postfixed 20 min in 4% paraformaldehyde (PFA 4%, Sigma-Aldrich). Slices were blocked 2 hours at room temperature with PBS-0.5% Triton X100 (Sigma-Aldrich)-3% bovine serum albumin (BSA, Sigma-Aldrich) and then incubated overnight at 4 °C with the following primary antibodies: rat endothelial cell antigen (RECA-1; MCA970, 0.4 mg mL^{-1}, BioRad, Marnes-la-Coquette, France) in PBS-0.5% Triton X100-1% BSA. Primary antibody was detected with an Alexa-555-conjugated goat anti-mouse immunoglobulin G (1 mg mL^{-1}; A-21434, Invitrogen, Carlsbad, CA, USA) in PBS-0.5% Triton X100-1% BSA containing Hoechst 33342 (10 µg mL^{-1}, Sigma-Aldrich). Subsequently, slices were cover slipped with the mounting medium Aqua-PolyMount (Tebu-Bio, Le Perray-en-Yvelines, France) and acquired at ×20 magnification using epifluorescence microscope Leica DMi8S (Leitz Leica, Wetzlar, Germany).

Energy dispersive X-ray analysis (EDX)

At the end of the experiments, animals were euthanized under anaesthesia and brain tumor, healthy brain hemisphere, liver, and kidney were dried overnight at 100 °C before undergoing a calcination step at 600 °C for 1 hour. The analysis of the samples was then conducted using two Bruker XFLASH 6/30 EDX cameras.

Results and discussion

Physicochemical characterization of [^{64}Cu]-FAU nanosized zeolite

The main physicochemical properties of nanosized Na-FAU and [^{64}Cu]-FAU zeolite samples after ion exchange are presented in Fig. 2. The X-ray diffraction patterns of as-prepared Na-FAU and ion-exchanged [^{64}Cu]-FAU are presented in Fig. 2A. These XRD patterns revealed the Bragg peaks corres-

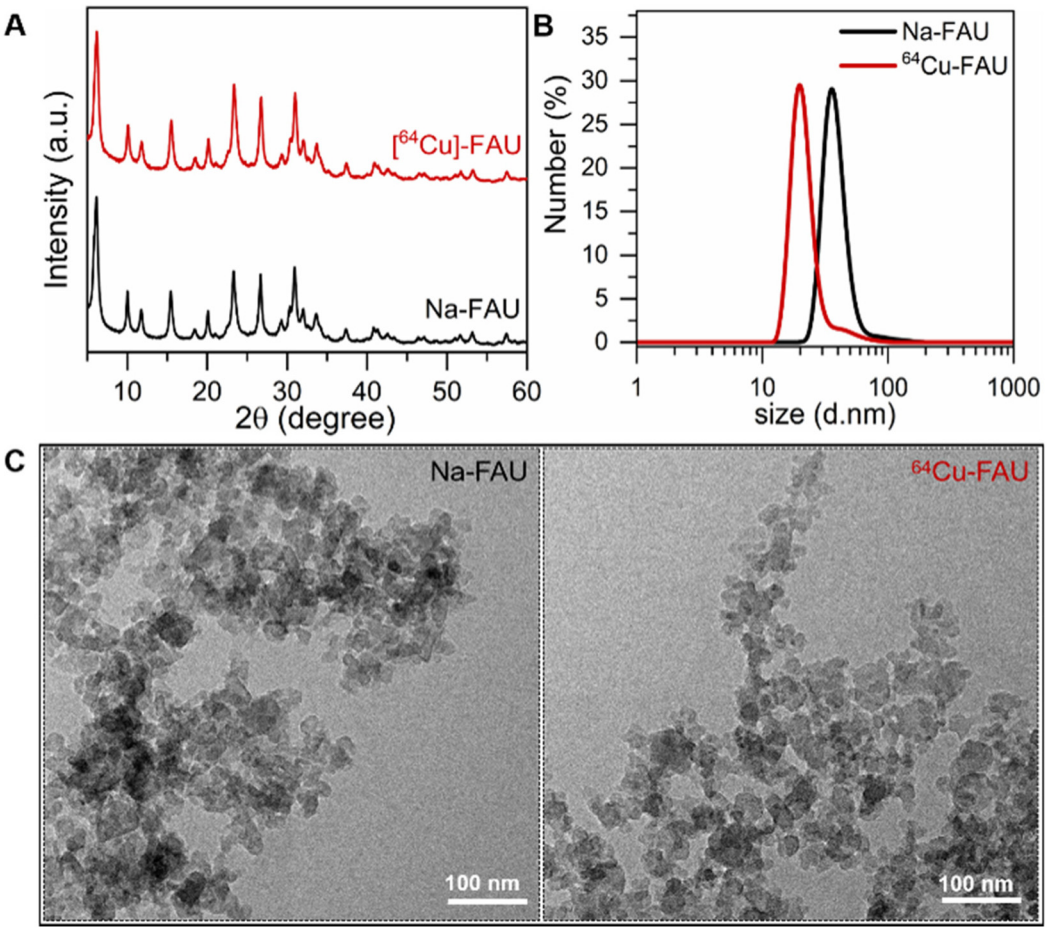

Fig. 2 (A) Powder XRD patterns of Na-FAU and [^{64}Cu]-FAU nanosized zeolites. (B) Dynamic light scattering curves of Na-FAU and [^{64}Cu]-FAU. (C) TEM images of Na-FAU and [^{64}Cu]-FAU nanocrystals.

ponding to pure highly crystalline FAU zeolite samples. The relatively broad peaks observed in these XRD patterns originate from the small size of the zeolite crystals. These findings were confirmed through TEM analysis (Fig. 2C), which revealed the size of zeolite particles of 30 nm.

A comprehensive examination of both particle size distribution and colloidal stability was undertaken on the colloidal suspensions containing Na-FAU and [^{64}Cu]-FAU by DLS (Fig. 2B). The DLS analysis revealed an average hydrodynamic particle diameter of 35 nm. The Na-FAU and [^{64}Cu]-FAU colloidal suspensions with zeta potential values of −38 mV and −40 mV, respectively were used. The negative zeta potential values confirmed the negatively surface charge of the zeolite nanoparticles in the suspensions. The suspensions containing highly crystalline zeolite nanoparticles with negative surface charge and strong repulsion between them remained stable for over three months without sedimentation. Both the DLS and zeta potential measurements are consistent with the visual observation of the stable suspensions. No change in the size and surface charge of zeolite nanoparticles over time was observed thus affirming their suitability for *in vivo* applications. The suspensions containing highly crystalline zeolite

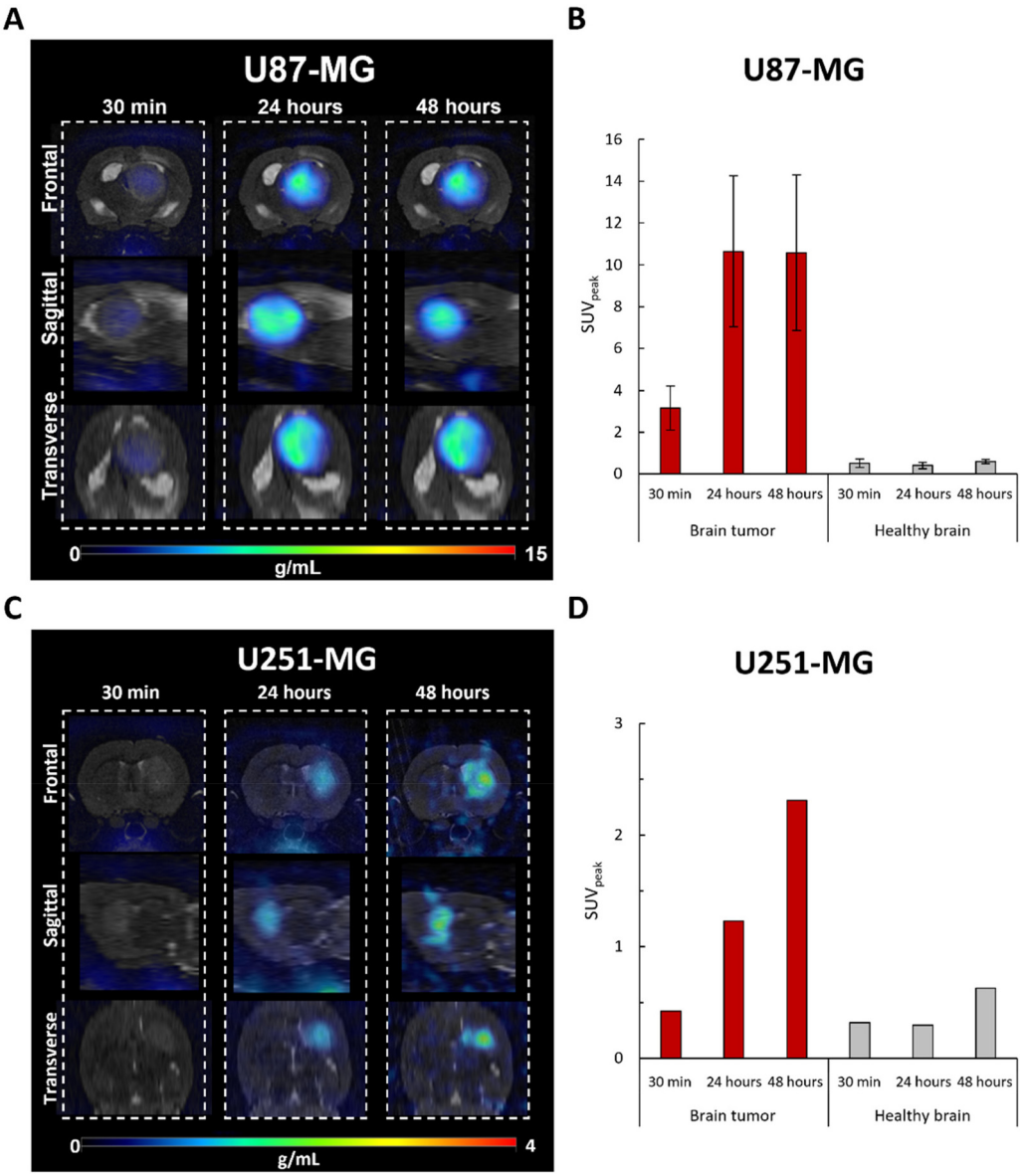

Fig. 3 (A) Representative images of merged anatomical *T*2w-MRI and [^{64}Cu]-FAU PET centered on head at 30 min, 24 hours and 48 hours post-injection in the U87-MG GBM model. (B) Quantification of [^{64}Cu]-FAU uptake by SUV$_{peak}$ in U87-MG brain tumor and healthy contralateral hemisphere at 30 min, 24 hours and 48 hours post-injection. Mean ± SD, n = 3. (C) Representative images of merge anatomical *T*2w MRI and [^{64}Cu]-FAU PET centered on head at 30 min, 24 hours and 48 hours post-injection in U251-MG GBM model. (D) Quantification of [^{64}Cu]-FAU uptake by SUV$_{peak}$ in U251-MG brain tumor and healthy contralateral hemisphere at 30 min, 24 hours and 48 hours post-injection. n = 1.

nanoparticles with negative surface charge and strong repulsion between them remained stable for over three months without sedimentation (ESI Fig. 1 and 2†).

The chemical composition of [^{64}Cu]-FAU zeolite was determined by ICP analysis; the Si/Al ratio of the nanocrystals is 1.3. This ratio remained unchanged even after the ion exchange process. The presence of copper determined by ICP analysis revealed the trace amount of 0.0014 wt%. The radioactivity of the suspension containing [^{64}Cu]-FAU zeolite was measured to be 474 MBq in 4 mL.

In vivo PET imaging studies

Brain imaging. The [^{64}Cu]-FAU was intravenously injected into GBM-bearing nude rats, and PET imaging was performed at 30 min, 24 hours, and 48 hours post-injection. In the U87-MG brain tumor model, a rapid and gradual accumulation over time was observed. After 30 min of the zeolites injection, the SUV_{peak} in the tumor was measured to be 3.16 ± 1.05, whereas the SUV_{peak} in the healthy brain was 0.51 ± 0.20. Time activity curve in a representative rat bearing a U87-MG model, reveals a rapid accumulation in the tumor occurring between injection and 10 min post-injection (ESI Fig. 3†). At 24 and 48 hours post-injection, the PET analysis showed higher SUV_{peak} value in the tumor core of 10.65 ± 3.61 and 10.58 ± 3.72, respectively. While the SUV_{peak} in the healthy brain was measured to be 0.40 ± 0.15 and 0.59 ± 0.10 after 24 hours and 48 hours, respectively (Fig. 3A and B). Interestingly, in the U251-MG model, a lower uptake occurred, with almost no uptake detected at 30 min but clearly visible at 24 hours and increasing up to 48 hours. This resulted in a SUV_{peak} in the tumor of 0.42, 1.22 and 2.31 at 30 min, 24 hours and 48 hours, respectively, compared to 0.32, 0.29, and 0.63 in the healthy brain at the same time (Fig. 3C and D). These results suggest a rapid accumulation of nanozeolites in the U87-MG brain tumor during the first 24 hours, which then remained stable over time. For the U251-MG tumor, the lower but increasing radioactivity rather suggested a progressive uptake with time. However, although the study was performed with a limited number of rats for U251-MG model (n = 1), the difference of SUV_{peak} values and, more importantly, the kinetics allow us to suggest a difference between U87-MG and U251-MG models.

Consistent with our previous results with MRI,[4] these findings confirm that FAU nanoparticles demonstrate high targeting abilities, as they exhibited prolonged accumulation at the tumor site while minimizing accumulation in the healthy brain. Interestingly, shown for the first time, the extended tumor retention of the [^{64}Cu]-FAU nanoparticles (at least 48 hours) enhances their potential for targeted therapy as drug carriers or radiosensitizers. It reinforces the special interest in using nanozeolites since with other particles, after the initial uptake a decline was reported after 24 hours in the U87-MG model.[21,22]

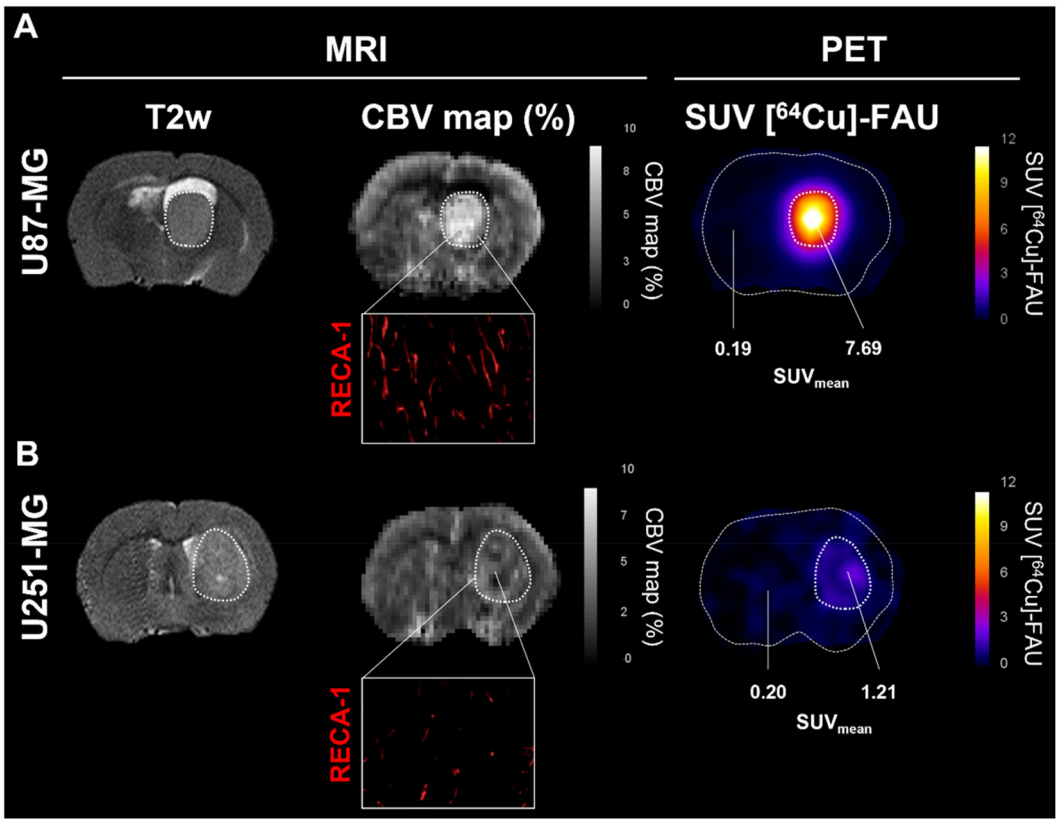

Fig. 4 Representative images of anatomical *T*2w MRI, maps of CBV and [^{64}Cu]-FAU PET at 24 hours in (A) U87-MG and (B) U251-MG GBM models. Representative images of RECA-1 immunostaining (red) are shown as insets for each preclinical GBM model.

Although zeolite retention was observed in both glioblastoma models, the U87-MG and U251-MG tumors imply differences in uptake, both in quantity and adsorption kinetics. This opens the question of whether the prospective difference in the tumor targeting between both models could be related to a difference in the vascularization, as shown by Corroyer-Dulmont *et al.*[23]

The cerebral blood volume (CBV) was measured with MRI (Fig. 4). Observation of CBV maps revealed higher vascularization in both tumor models compared to the contralateral healthy tissues. However, a significant difference between U87-MG (Fig. 4A) and U251-MG (Fig. 4B) models was also observed. The relative CBV was higher in the U87-MG model (2.59 ± 0.34) compared to the U251-MG model (1.36), which is in line with our previous reports.[23] Immunohistofluorescence analyses with rat endothelial cell antigen (RECA-1) depicted tortuous vessels with an abnormal shape, a well-known feature of tumor vessels. Consistent with the MRI measurement, the tumor in the U87-MG exhibited a higher vessels density than the U251-MG (Fig. 4A, Inset in B). These findings are in a good agreement with our previous results that showed a greater cerebral blood volume for the U87-MG model relative to the U251-MG model.[23] The new findings suggest that a relationship between the tumor vascularization and the amount of zeolite nanoparticles accumulated exist. Previous studies described no difference in vascular permeability (Ktrans), while per-

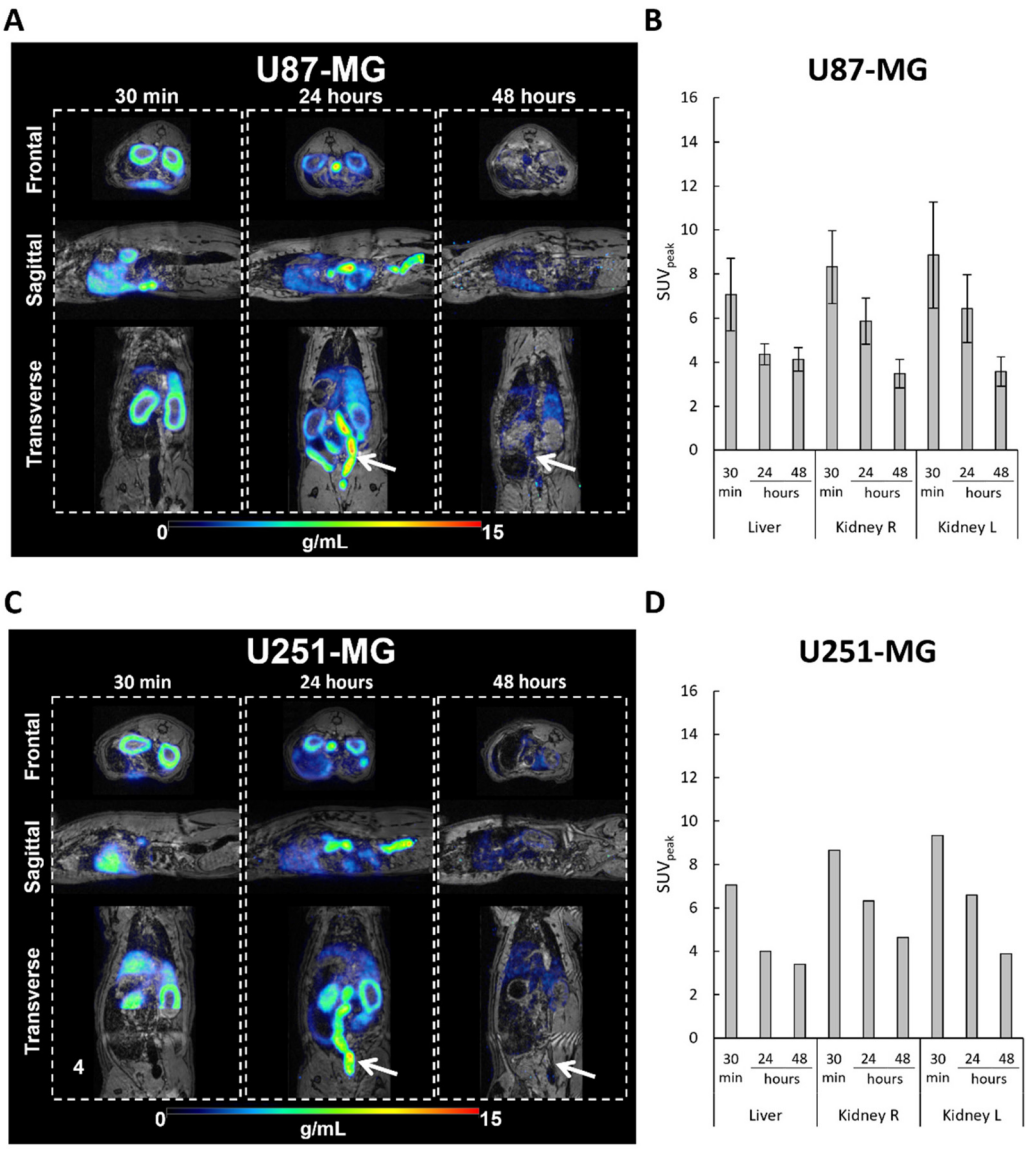

Fig. 5 (A) Representative images of merged anatomical *T*2w MRI and [^{64}Cu]-FAU PET centered on body at 30 min, 24 hours and 48 hours post-injection in U87-MG-bearing rat. (B) Quantification of [^{64}Cu]-FAU uptake by SUV_{peak} in liver and kidney in U87-MG-bearing rat at 30 min, 24 hours and 48 hours post-injection. Mean ± SD, n = 3. (C) Representative images of merge anatomical *T*2w MRI and [^{64}Cu]-FAU PET centered on body at 30 min, 24 hours and 48 hours post-injection in U251-MG-bearing rat. (D) Quantification of [^{64}Cu]-FAU uptake by SUV_{peak} in liver and kidney in U251-MG-bearing rat at 30 min, 24 hours and 48 hours post-injection. n = 1.

fusion tended to be higher in U87-MG tumors compared to U251-MG tumors.[23,24] This parameter could explain the difference in uptake between both models. Indeed, Fan *et al.*, identified tumor blood flow as a crucial factor in nanoparticles delivery and demonstrated that high perfusion improves nanoparticles delivery.[25]

Whole body imaging. A great advantage of PET imaging is that is allows whole-body imaging. Therefore, we assessed the location of the nanoparticles in the body after IV injections of [^{64}Cu]-FAU.

An elevated level of radioactivity was observed in the kidney (cortex) and liver in rat bearing the U87-MG tumors in the brain, at 30 min post-injection of [^{64}Cu]-FAU, with SUV_{peak} values of 7.06 ± 1.64 and 8.32 ± 1.64, respectively (Fig. 5A and B). Similar results were observed in the rat bearing the U251-MG brain tumor; the SUV_{peak} of 7.07 and 8.64 in the kidney and liver, respectively measured (Fig. 5C and D). While in the U87-MG model, PET images showed a decrease in activity both in the liver and in the kidney at 24 hours and 48 hours post-injection compared to the 30 min. Fig. 5B shows the SUV_{peak} of 4.35 ± 0.47 and 6.42 ± 1.53 at 24 hours, and 4.12 ± 0.53 and 3.57 ± 0.66 at 48 hours for liver and kidney, respectively. In the U251-MG model, similar results were obtained, the SUV_{peak} in the liver decreased from 4.00 at 24 hours to 3.39 at 48 hours, whileSUV_{peak} in the kidney decreased from 6.60 at 24 hours to 3.88 at 48 hours (Fig. 5D).

These results clearly demonstrate the elimination of [^{64}Cu]-FAU zeolite nanoparticles, which was similar in rats bearing both GBM models. The observed radioactivity in the kidney, particularly in the kidney cortex, suggests that [^{64}Cu]-FAU nanoparticles cannot penetrate the glomerular filtration barrier of the kidney. These observations are in a good agreement with previous studies showing that particles with a size larger than 8 nm cannot be cleared *via* kidney and urine.[26] In fact, glutathione coated copper nanoparticles with an average diameter of 2.0 ± 0.4 nm, were found in the kidney and subsequently in the bladder and not limited to the cortex.[27] Moreover, our results strongly support that [^{64}Cu] ions remain within the zeolite nanoparticles and do not leach. In addition, the activity of the [^{64}Cu]-FAU in the liver, the gastrointestinal tract, and feces (indicated by white arrows) suggests a hepatobiliary elimination of nanoparticles as shown in Fig. 5A and C at 24 hours, and to a lesser extent at 48 hours. These results are in a good agreement with earlier work published by Poon *et al.*[28]

The accumulation of [^{64}Cu]-FAU in the tumor and peripheral organs was clearly demonstrated in PET imaging. To further confirm these *in vivo* biodistribution, γ-counting was performed at 48 hours on several tissues. As shown in Fig. 6A, the uptake of [^{64}Cu]-FAU nanoparticles in the U87-MG tumor was calculated to be 4.80 %ID g^{-1} at 48 hours post-injection. On the other hand, uptake in the contralateral healthy brain remained below 0.03 %ID g^{-1}. These results reinforce the conclusion that the tumor-specific accumulation of [^{64}Cu]-FAU relative to the normal healthy tissue.

In line with PET imaging results in U87-MG bearing brain tumor rats, the uptake of [^{64}Cu]-FAU in the other organs was lower than in the tumor. The [^{64}Cu]-FAU uptake values of 1.51, 1.22, 0.33, 0.32, 0.31 and 0.25 %ID g^{-1} in liver, kidney, lung, heart, spleen and blood, respectively were measured (Fig. 6A). Similar results in U251-MG models were measured that are in agreement with the PET results. The tumor uptake was lower than that in the liver and kidney at 48 hours as shown in Fig. 6B.

To assess a possible leaching of [^{64}Cu] from the zeolite nanocrystals and to confirm that the activity is associated with the [^{64}Cu]-FAU zeolite and not to the free [^{64}Cu] ions leached from the zeolite, rats were euthanized and the organs (brain

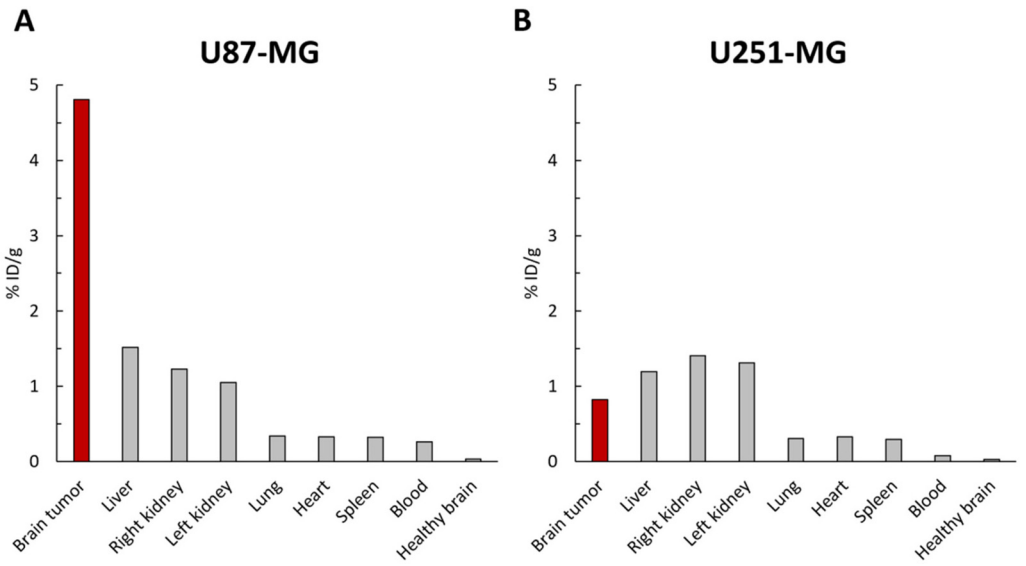

Fig. 6 Biodistribution (%ID g^{-1}) of [^{64}Cu]-FAU in tumor and principal organs 48 hours after tail vein injection in (A) U87-MG and (B) U251-MG-bearing rats. The %ID g^{-1} is defined as percentage of total injected dose per gram tissue weight.

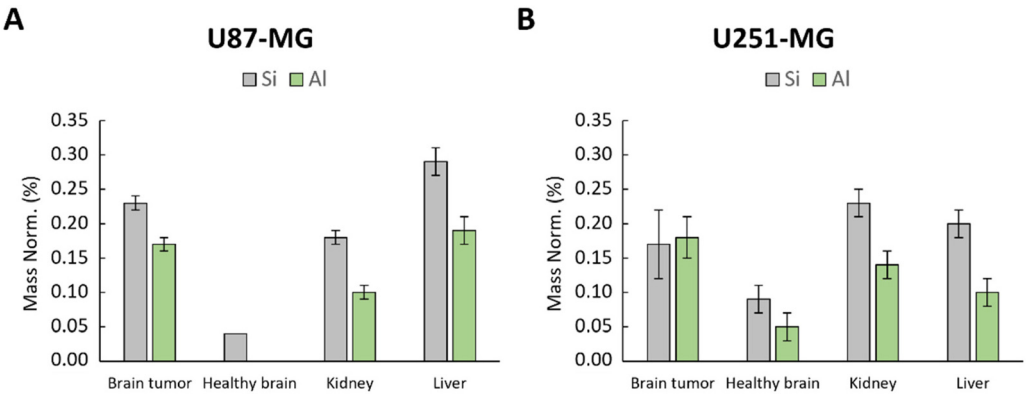

Fig. 7 EDX analysis of healthy brain, kidney and brain tumor in (A) U87-MG and (B) U251-MG models; Si and Al content represented by grey and green bars, respectively characteristic of zeolite.

tumor, healthy brain, liver and kidney) were collected and subjected to EDX analysis. The Si and Al-contents in these organs at 24 hours post-injection of [^{64}Cu]-FAU zeolite were determined (Fig. 7). EDX provided valuable information on the distribution and amounts of Si and Al elements, within the studied organs.

As depicted in Fig. 7, the amount of Si and Al were notably higher in the tumors, kidney and liver. Conversely, in the contralateral healthy brain of U87-MG model, only a small amount of Si was detected without the presence of Al (Fig. 7A). In the healthy brain of U251-MG bearing rat (Fig. 7B), EDX showed low quantity of Si and Al compared to the U87-MG brain tumor. These findings strongly suggest that the zeolite nanocrystals built of Si and Al, either are not present or present in negligible low amount in the healthy brain, which is in a good agreement with the PET imaging data. These results reinforce the conclusion that the [^{64}Cu]-FAU nanoparticles are specifically accumulated in the tumor relative to the normal brain thus indicating the successful targeting.

Conclusion

In summary, we have prepared [^{64}Cu]-FAU zeolite nanoparticles by ion exchange approach using Na-FAU zeolite. The Na-FAU zeolite was exchanged with radioactive [^{64}Cu]-Cl_2 in water colloidal suspensions. The [^{64}Cu]-FAU zeolite nanoparticles were used as the radiotracer for accurate monitoring of their *in vivo* biodistributions by PET imaging. One main advantage of our strategy is that PET imaging provides absolute quantification of the [^{64}Cu]-FAU nanoparticles which is not possible with other techniques including fluorescence and bioluminescence.

The *in vivo* tracking of the [^{64}Cu]-FAU zeolite nanocrystals in glioblastoma-bearing rats using PET imaging after intravenous administration (24 MBq or 5–20 mg kg^{-1} of zeolites) was investigated. PET acquisitions showed a rapid and specific tumor uptake in the U87-MG model reaching maximum activity at 24 hours, followed by a stabilization of the radioactivity for 48 hours. In the U251-MG glioblastoma model tumor uptake was gradual for at least 48 hours. No retention was observed in clearance organs (liver and kidney). Besides, the *ex vivo* analyses of the organs by EDX revealed the lower amount of Si and Al element coming from the zeolite nanoparticles in the healthy brain compared to the tumor. These results are in agreement with the PET findings. Thus, based on the biodistribution results, we firmly suggest that nanozeolites could serve as highly interesting tool for drugs, gases, or radiosensitizers due to their extended retention and specificity in tumors.

Author contributions

Conducted experiments: CH, AA, JT, OL, CA, FH, SV; experimental design: CH; AA; SM, SV; data analysis: CH, AA, CB, OL, SM, SV; animal care: CH, JT, CM; project supervision: SM, SV; manuscript writing: CH, AA, SM, SV; manuscript editing and reviewing: CH, AA, JT, CB, OL, CM, CA, MB, FH; SM, SV. All authors have read and agreed to the published version of the manuscript.

Conflicts of interest

There are no conflicts to declare.

Acknowledgements

The financial supports provided by French National Agency for Research “Investissements d’Avenir” no. ANR-11-LABEX-0018-01, the Région Normandie (Label of Excellence for the Centre for zeolites and nanoporous materials by the Region of Normandy (CLEAR) and RIN HYP-IRON2), the European Union-Fonds Européen de Développement Régional (FEDER), the Université Caen-Normandie, the Centre National de la Recherche Scientifique (CNRS Innovation), Institut National du Cancer (INCA-11699) are acknowledged.

References

1 A. L. Klein, G. Nugent, J. Cavendish, W. J. Geldenhuys, K. Sriram, D. Porter, R. Fladeland, P. R. Lockman and J. H. Sherman, *Pharmaceutics*, 2021, **13**, 948.
2 C. Tapeinos, M. Battaglini and G. Ciofani, *J. Control. Release Off. J. Control. Release Soc.*, 2017, **264**, 306–332.
3 H. Wang, J. Li, Y. Wang, X. Gong, X. Xu, J. Wang, Y. Li, X. Sha and Z. Zhang, *J. Controlled Release*, 2020, **319**, 25–45.
4 C. Anfray, S. Komaty, A. Corroyer-Dulmont, M. Zaarour, C. Helaine, H. Ozcelik, C. Allioux, J. Toutain, K. Goldyn, E. Petit, K. Bordji, M. Bernaudin, V. Valtchev, O. Touzani, S. Mintova and S. Valable, *Biomaterials*, 2020, **257**, 120249.
5 H. Awala, J.-P. Gilson, R. Retoux, P. Boullay, J.-M. Goupil, V. Valtchev and S. Mintova, *Nat. Mater.*, 2015, **14**, 447–451.
6 C. Helaine, H. Özçelik, S. Komaty, A. Amedlous, S. Ghojavand, D. Goux, R. Retoux, S. Mintova and S. Valable, *Colloids Surf., B*, 2022, **218**, 112732.
7 S. Mintova, M. Jaber and V. Valtchev, *Chem. Soc. Rev.*, 2015, **44**, 7207–7233.
8 V. Georgieva, C. Anfray, R. Retoux, V. Valtchev, S. Valable and S. Mintova, *Microporous Mesoporous Mater.*, 2016, **232**, 256–263.
9 K. Goldyn, C. Anfray, S. Komaty, V. Ruaux, C. Hélaine, R. Retoux, S. Valable, V. Valtchev and S. Mintova, *Microporous Mesoporous Mater.*, 2019, **280**, 271–276.
10 E. Csajbók, I. Bányai, L. Vander Elst, R. N. Muller, W. Zhou and J. A. Peters, *Chemistry*, 2005, **11**, 4799–4807.
11 A. Chakhoyan, J.-S. Guillamo, S. Collet, F. Kauffmann, N. Delcroix, E. Lechapt-Zalcman, J.-M. Constans, E. Petit, E. T. MacKenzie, L. Barré, M. Bernaudin, O. Touzani and S. Valable, *Sci. Rep.*, 2017, **7**, 10210.
12 J. P. Holland, R. Ferdani, C. J. Anderson and J. S. Lewis, *PET Clin.*, 2009, **4**, 49–67.
13 C. Qin, H. Liu, K. Chen, X. Hu, X. Ma, X. Lan, Y. Zhang and Z. Cheng, *J. Nucl. Med.*, 2014, **55**, 812–817.
14 L. Lattuada, A. Barge, G. Cravotto, G. B. Giovenzana and L. Tei, *Chem. Soc. Rev.*, 2011, **40**, 3019–3049.
15 M. M. Tsotsalas, K. Kopka, G. Luppi, S. Wagner, M. P. Law, M. Schäfers and L. De Cola, *ACS Nano*, 2010, **4**, 342–348.
16 A. Piotrowska, E. Leszczuk, F. Bruchertseifer, A. Morgenstern and A. Bilewicz, *J. Nanopart. Res.*, 2013, **15**, 2082.
17 A. Piotrowska, S. Męczyńska-Wielgosz, A. Majkowska-Pilip, P. Koźmiński, G. Wójciuk, E. Cędrowska, F. Bruchertseifer, A. Morgenstern, M. Kruszewski and A. Bilewicz, *Nucl. Med. Biol.*, 2017, **47**, 10–18.
18 S. Lacerda, W. Zhang, R. T. M. de Rosales, I. Da Silva, J. Sobilo, S. Lerondel, É. Tóth and K. Djanashvili, *ACS Appl. Mater. Interfaces*, 2022, **14**, 32788–32798.
19 S. Valable, B. Lemasson, R. Farion, M. Beaumont, C. Segebarth, C. Remy and E. L. Barbier, *NMR Biomed.*, 2008, **21**, 1043–1056.
20 M. Vanderhoek, S. B. Perlman and R. Jeraj, *J. Nucl. Med.*, 2012, **53**, 4–11.
21 R. Wang, X. Wang, J. Li, L. Di, J. Zhou and Y. Ding, *Bioact. Mater.*, 2022, **13**, 286–299.
22 J. Wang, H. Zhao, Z. Zhou, P. Zhou, Y. Yan, M. Wang, H. Yang, Y. Zhang and S. Yang, *ACS Appl. Mater. Interfaces*, 2016, **8**, 19872–19882.
23 A. Corroyer-Dulmont, E. A. Pérès, E. Petit, L. Durand, L. Marteau, J. Toutain, D. Divoux, S. Roussel, E. T. MacKenzie, L. Barré, M. Bernaudin and S. Valable, *Biol. Chem.*, 2013, **394**, 529–539.
24 J. J. Walsh, M. Parent, A. Akif, L. C. Adam, S. Maritim, S. K. Mishra, M. H. Khan, D. Coman and F. Hyder, *Front. Oncol.*, 2021, **11**, 692650.
25 F. Fan, B. Xie and L. Yang, *ACS Appl. Bio Mater.*, 2021, **4**, 7615–7625.
26 J. Wang and G. Liu, *Angew. Chem., Int. Ed.*, 2018, **57**, 3008–3010.
27 S. Yang, S. Sun, C. Zhou, G. Hao, J. Liu, S. Ramezani, M. Yu, X. Sun and J. Zheng, *Bioconjugate Chem.*, 2015, **26**, 511–519.
28 W. Poon, Y.-N. Zhang, B. Ouyang, B. R. Kingston, J. L. Y. Wu, S. Wilhelm and W. C. W. Chan, *ACS Nano*, 2019, **13**, 5785–5798.